JACS
JOURNAL OF THE AMERICAN CHEMICAL SOCIETY
pubs.acs.org/JACS
Article

Environmentally Benign and Long Cycling Mn-Ion Full Batteries Enabled by Hydrated Eutectic Electrolytes and Polycarbonyl Conjugated Organic Anodes

Tengfei Dai, Binze Yang, Jie Wei, Xinmei Song, Pengbo Zhang, Yuzhu Liu, Sheng Wen, Huan Li, Tianchen Yu, Zuoxiu Tie, Huapeng Sun, Yichao Yan,* and Zhong Jin*

Cite This: J. Am. Chem. Soc. 2025, 147, 13721−13731

Read Online

ACCESS | Metrics & More | Article Recommendations | Supporting Information

ABSTRACT: Aqueous rechargeable manganese (Mn)-ion batteries have recently emerged as a promising candidate for multivalent ion rechargeable batteries. However, challenges remain, particularly in expanding the electrolyte's voltage window and identifying compatible anode materials. Herein, we introduce a Mn-ion full battery comprising a nickel hexacyanoferrate (NiHCF) cathode, a perylene-3,4,9,10-tetracarboxylic diimide (PTCDI) anode, and a novel hydrated eutectic electrolyte formulated from $Mn(ClO_4)_2{\cdot}6H_2O$ and acetamide. This electrolyte composition, optimized for molar ratio, provides a stable solvation structure that suppresses water reactivity and supports high ionic conductivity, as confirmed by spectroscopic and molecular dynamics analyses. The PTCDI anode facilitates highly reversible Mn^{2+} storage via a unique enolization redox reaction, delivering exceptional rate capability and cycling stability. As a result, the NiHCF||PTCDI full battery achieves a 1.2 V plateau, excellent rate performance (up to 5.0 A g^{-1}), and long cycling life with 95.6% capacity retention over 1200 cycles at 1.0 A g^{-1}. This study proposes a feasible strategy for the construction of environment-friendly, long-life and low-cost aqueous Mn-ion full batteries, offering a sustainable and high-performance solution for future energy storage applications.

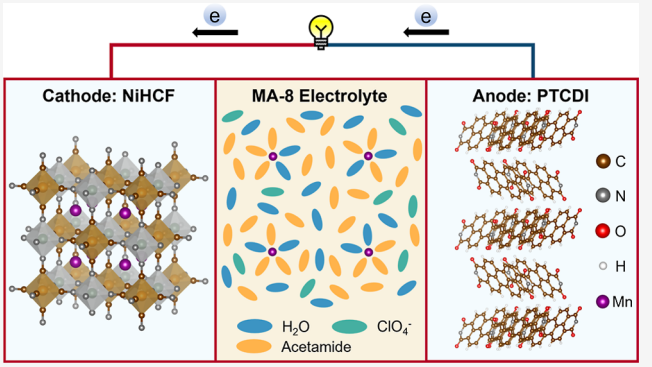

INTRODUCTION

The rapid success of lithium-ion (Li^+) batteries in powering portable electronics, electric vehicles, and grid storage has fueled unprecedented growth in the energy storage market.[1−4] However, the extensive demand for Li-ion technology has raised critical issues around sustainability, including limited lithium reserves, high extraction costs, and the use of flammable organic electrolytes.[5−7] These factors underscore the urgent need for alternative battery technologies that can deliver comparable performance with greater environmental compatibility, reduced costs, and enhanced safety.[8,9] In this context, aqueous multivalent ion batteries have emerged as a promising alternative due to their use of earth-abundant elements, minimal toxicity, and intrinsic safety.[10−12]

Among multivalent ions,[13−17] manganese (Mn) is especially promising due to its high natural abundance, low cost, and nontoxicity.[18,19] The ionic radius of Mn^{2+} (0.81 Å) is close to that of Zn^{2+} (0.74 Å), allowing Mn^{2+} ions to be readily accommodated by many Zn-compatible host compounds.[20] Additionally, Mn exhibits a low redox potential of −1.19 V versus standard hydrogen electrode (SHE) and a high theoretical capacity (976 mAh g^{-1}), making Mn-ion batteries an attractive candidate for rechargeable multivalent ion batteries.[21] Recent efforts have demonstrated high-voltage aqueous Mn-ion batteries by pairing Mn metal anodes with materials like $Mn_{0.18}V_2O_5{\cdot}nH_2O$, $Al_{0.1}V_2O_5{\cdot}1.5H_2O$, and tetrachloro-1,4-benzoquinone.[22,23] Besides Mn metal, other Mn^{2+} hosting compounds have also been used as anode materials for Mn-ion batteries. Intercalation-type anodes, such as Mo_6S_8, often lack the stability required in aqueous Mn-ion systems.[24] Organic molecules with carbonyl groups, such as PI-COF, represent a promising class of materials due to their ability to undergo reversible redox reactions.[25] The carbonyl groups in PI-COF enable Mn^{2+} storage, while its π-conjugated structure supports cycling stability and compatibility with aqueous systems.

Although Mn-based aqueous batteries show great potential, critical obstacles, particularly in electrolyte and anode design, have hindered their practical applications. For example, in aqueous electrolytes, unavoidable side reactions, such as

Received: January 26, 2025
Revised: April 6, 2025
Accepted: April 8, 2025
Published: April 14, 2025

https://doi.org/10.1021/jacs.5c01639
J. Am. Chem. Soc. 2025, 147, 13721−13731

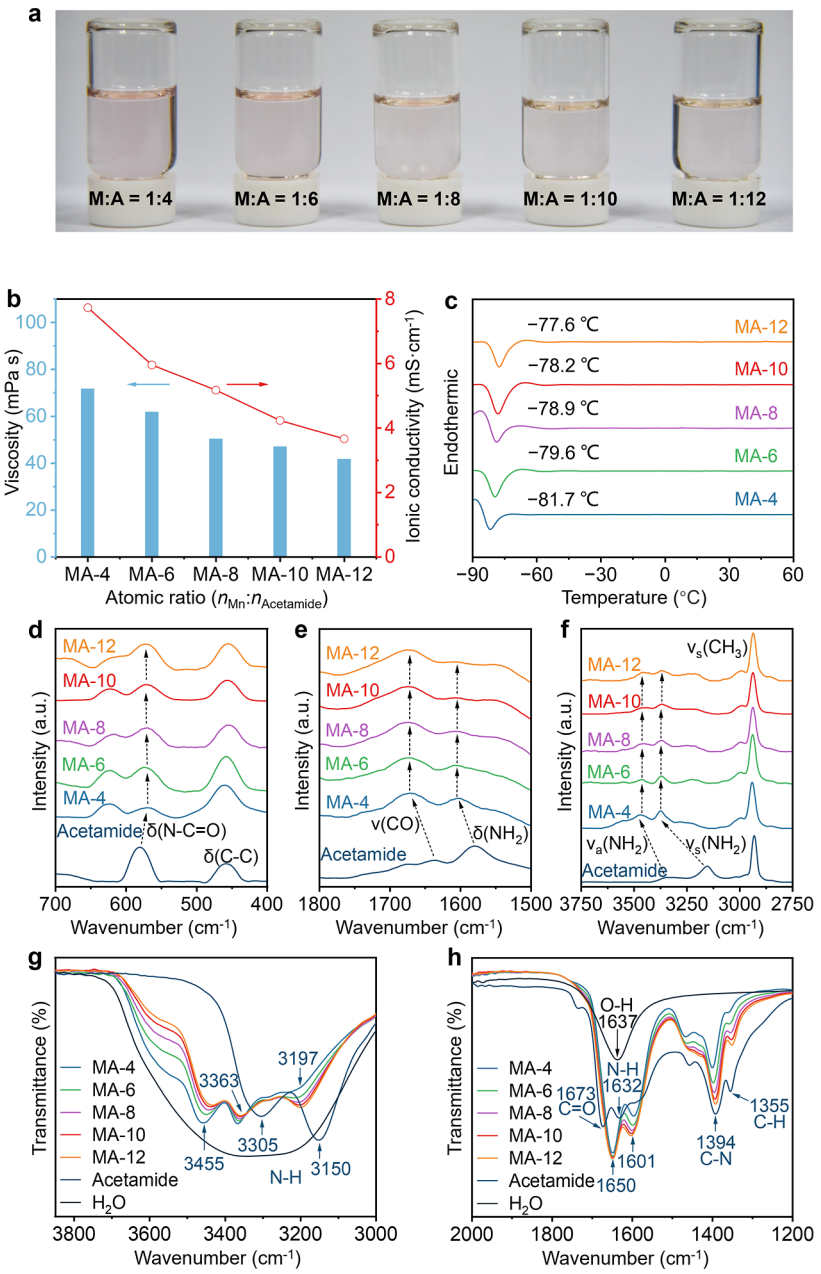

Figure 1. (a) Optical photographs of the Mn-ion eutectic electrolytes with different mole ratios of $n_{Mn^{2+}}/n_{acetamide}$ (MA-4 = 1:4; MA-6 = 1:6; MA-8 = 1:8; MA-10 = 1:10; MA-12 = 1:12). (b) Viscosity and ionic conductivity and (c) DSC data of MA-4, MA-6, MA-8, MA-10 and MA-12 electrolytes. (d−f) Raman spectra of acetamide and the Mn-ion eutectic electrolytes. (g,h) FTIR spectra of H_2O, acetamide, MA-4, MA-6, MA-8, MA-10, and MA-12, respectively.

hydrogen evolution, limit the electrochemical stability window (ESW) and compromise battery performance over extended cycles.[20−24] Efforts to overcome these limitations have focused on developing specialized electrolytes that minimize water reactivity.[24,26,27] Hydrated eutectic electrolytes, which consist of metal salts and organic compounds in a stable, room-temperature liquid form, are particularly promising.[28−31] These electrolytes can expand the ESW by reducing water's reactivity through controlled hydration, thus limiting side reactions like hydrogen evolution.[32−34] In hydrated eutectic systems, the structural water content from the metal salt enables high ionic conductivity while limiting free water molecules, thereby suppressing unwanted electrochemical reactions.[35−37] Consequently, these electrolytes provide an effective strategy to enhance the stability of Mn-ion batteries, particularly during Mn coordination and dissociation processes. Acetamide is a low-cost, environmentally benign, and chemically stable eutectic solvent, offering intriguing capability to coordinate with metal cations through its carbonyl group.[38] The carbonyl group in acetamide acts as an electron donor, while the amide group in acetamide serves as an electron acceptor, forming strong hydrogen bonds with structural water molecules in $Mn(ClO_4)_2{\cdot}6H_2O$. This interaction significantly reduces water reactivity and modifies the hydrogen-bonding network.[39]

In this work, we present a novel Mn-ion full battery incorporating a NiHCF cathode, a PTCDI anode, and a tailored hydrated eutectic electrolyte consisting of $Mn(ClO_4)_2{\cdot}6H_2O$ and acetamide. By optimizing the Mn-to-acetamide

https://doi.org/10.1021/jacs.5c01639
J. Am. Chem. Soc. 2025, 147, 13721−13731

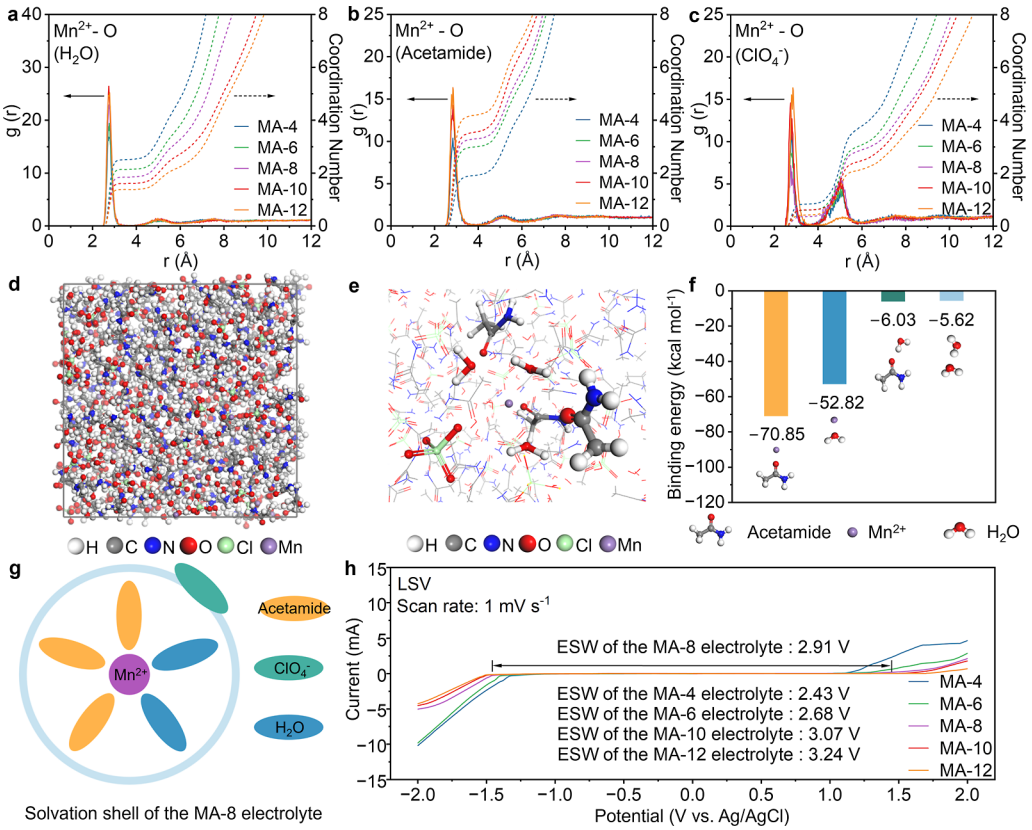

Figure 2. (a–c) Radial distribution functions for Mn^{2+}–O (H_2O), Mn^{2+}–O (acetamide), and Mn^{2+}–O (ClO_4^-) obtained by molecular dynamics simulations of the MA-4, MA-6, MA-8, MA-10, and MA-12 electrolytes. (d) 3D snapshot of the MA-8 electrolyte by molecular dynamics simulations and (e) possible Mn^{2+}-solvation structure in the MA-8 electrolyte. (f) Binding energy for Mn^{2+} with acetamide, Mn^{2+} with H_2O, acetamide with H_2O, and H_2O with H_2O. (g) Schematic illustration of solvation shell of the MA-8 electrolyte. (h) LSV curves of the MA-4, MA-6, MA-8, MA-10, and MA-12 electrolytes.

molar ratio, we create a solvation structure with high ionic conductivity, low viscosity, and reduced water reactivity. Spectroscopic analysis and molecular dynamics simulations reveal a stable solvation shell that enhances Mn^{2+} transport and mitigates side reactions. The PTCDI anode, compatible with this eutectic electrolyte, supports Mn^{2+} storage through a reversible enolization redox reaction, achieving high stability and efficient cycling performance. Consequently, the PTCDI electrode, when assembled with the Mn-ion eutectic electrolyte, successfully exhibits good rate performance and high cycling stability. Together, these advancements enable a full cell with a stable 1.2 V voltage plateau, excellent rate capability (up to 5.0 A g^{-1}), and exceptional cycling stability, maintaining 95.6% capacity retention after 1200 cycles at 1.0 A g^{-1}. This work demonstrates a practical pathway for Mn-ion batteries by integrating a hydrated eutectic electrolyte with an innovative organic anode. Our findings advance Mn-ion battery technology, highlighting its potential as a sustainable, high-performance alternative for scalable energy storage applications.

RESULTS AND DISCUSSION

Preparation and Spectroscopic Characterizations of Mn-Ion Eutectic Electrolytes. This study developed hydrated Mn-ion eutectic electrolytes using acetamide as the solvent to investigate its role in rechargeable Mn-ion batteries. The molar ratios of Mn^{2+} to acetamide ($n_{Mn^{2+}}/n_{acetamide}$) were varied to prepare different electrolytes, denoted as MA-4 (e.g., 1:4), MA-6, MA-8, MA-10, and MA-12 (Figure 1a). The eutectic frameworks formed through Lewis acid–base interactions between Mn^{2+} and acetamide provide the basis for effective electrolyte performance (Figure S1). Notably, no additional water was introduced, with only the structural water in $Mn(ClO_4)_2{\cdot}6H_2O$ present (Figure S2). Viscosity and ionic conductivity trends (Figure 1b) reveal a decrease in viscosity and ionic conductivity with increasing acetamide content, indicating more favorable ion mobility at higher acetamide levels. Differential scanning calorimetry (DSC) data (Figure 1c) show a slight increase in melting point with acetamide, attributed to the charge delocalization between $Mn(ClO_4)_2{\cdot}6H_2O$ and acetamide. The flame retardancy of MA-8 and MA-12 was confirmed by flammability testing (Figure S3), showcasing their stability under potential operational conditions.

Spectroscopic analyses, including Raman (Figure 1d–f) and FTIR spectra (Figure 1g,h), were conducted to explore the molecular interactions between acetamide and H_2O in the reconstructed hydrogen-bonding network of the Mn-ion eutectic electrolytes. In the Raman spectra (Figure 1d), the asymmetric deformation vibration of the amide δ(N–C=O) appears at 570 cm^{-1}, shifted from 581 cm^{-1} signifying the newly constructed hydrogen-bonding network. Figure 1e shows the stretching vibration of carbonyl group ν(C=O) and the bending vibration of the amine group $\delta(NH_2)$ shift slightly toward higher wavenumbers, indicating coordination between Mn^{2+} and carbonyl groups within electrolytes. Figure

https://doi.org/10.1021/jacs.5c01639
J. Am. Chem. Soc. 2025, 147, 13721–13731

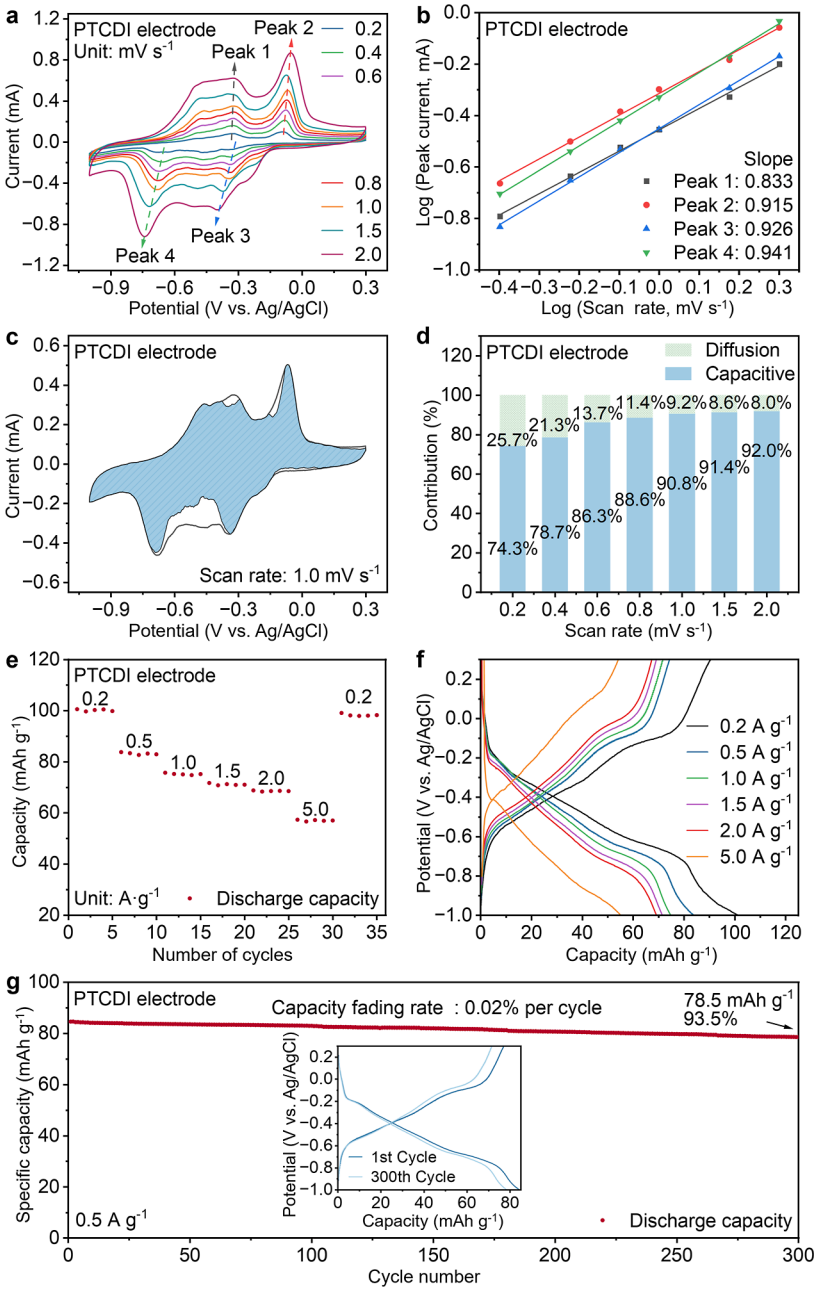

Figure 3. (a) CV curves of the PTCDI electrode at different scan rates (0.2−2.0 mV s^{-1}). (b) Log (peak current) versus Log (scan rate) plots for four redox peaks. (c) Pseudocapacitive contribution (the shaded region) to the total capacity of the PTCDI electrode at 1.0 mV s^{-1}. (d) Column chart of the rate-dependent capacity contributions from diffusion-limited and capacitive-controlled processes of the PTCDI electrode. (e) Rate performance and (f) galvanostatic charge−discharge profiles of the PTCDI electrode at different current densities. (g) Cycling performance of the PTCDI electrode at a current density of 0.5 A g^{-1}.

1f further illustrates the symmetric and asymmetric stretching vibrations of the amine group shift distinctly toward higher wavenumbers reinforcing the role of acetamide and H_2O in restructuring the hydrogen-bonding network. In the FTIR spectra (Figure 1g), the strong band at 3455 cm^{-1} is assigned to the O−H stretching vibration of the structural water in the $Mn(ClO_4)_2{\cdot}6H_2O$. The intensity of this band significantly decreases with acetamide addition, indicating reduced free water activity. Additionally, two intense bands of N−H stretching vibration of acetamide shift toward higher wavenumbers, suggesting disruption and reconfiguration of water clusters' hydrogen bonding upon forming hydrated eutectic electrolytes. Figure 1h shows shifts in the carbonyl group's stretching vibration from 1673 to 1650 cm^{-1} and the bending vibration of amine group in acetamide from 1632 to 1601 cm^{-1}, confirming interactions between Mn^{2+} and carbonyl groups in the Mn-ion eutectic electrolytes.

Solvation Structure Analyses of Mn-Ion Eutectic Electrolytes and Electrochemical Properties. Molecular dynamics simulations were conducted to analyze the radial distribution functions and solvation structure among H_2O, acetamide and perchlorate ion (ClO_4^-) in the Mn-ion eutectic electrolytes (Figure 2a−e). In Figure 2a, the Mn^{2+}−O (H_2O) coordination numbers of MA-4, MA-6, MA-8, MA-10, and MA-12 are 2.74, 2.34, 2.31, 2.23, and 1.91, respectively. In Figure 2b, the Mn^{2+}−O (acetamide) coordination number for

https://doi.org/10.1021/jacs.5c01639
J. Am. Chem. Soc. 2025, 147, 13721−13731

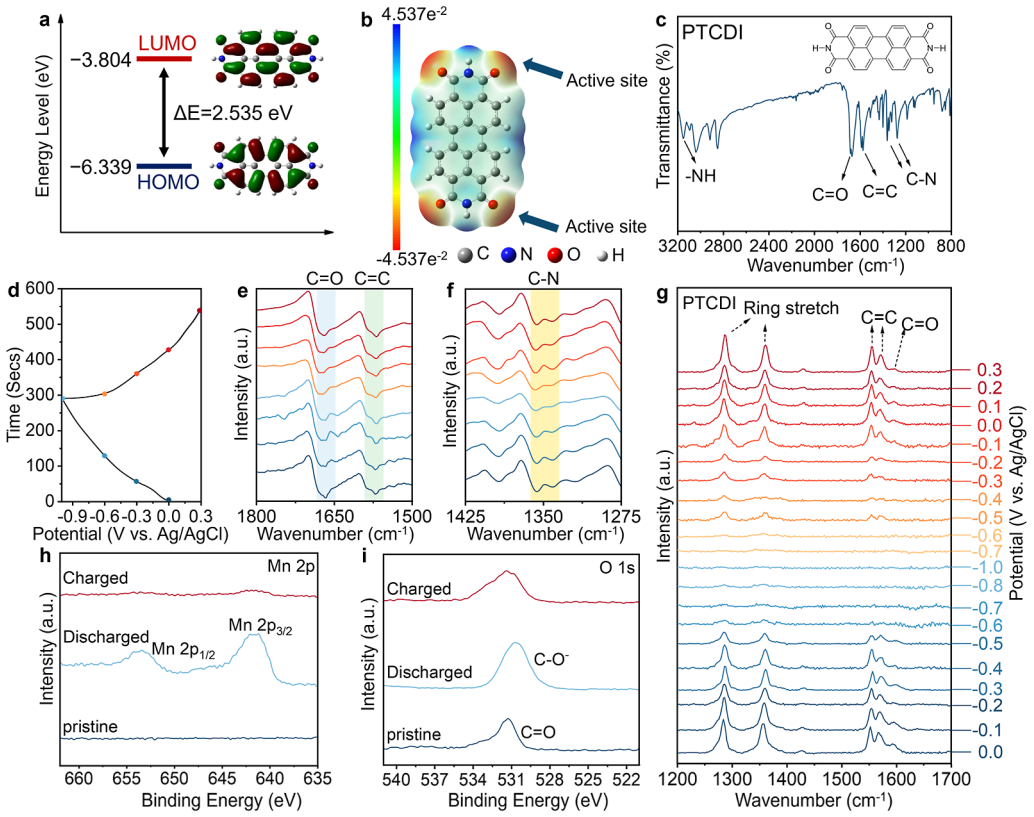

Figure 4. (a) Calculated HOMO and LUMO energy levels and band gaps of PTCDI. (b) The electrostatic potential calculations of PTCDI. (c) FTIR spectrum of PTCDI. (d) The charge−discharge profile and (e,f) corresponding ex situ FTIR spectra of PTCDI electrodes. (g) In situ Raman spectra of the PTCDI electrode in the MA-8 electrolyte during the charge/discharge processes. Ex situ XPS spectra at (h) Mn 2p, and (i) O 1s regions of PTCDI electrodes at different charged/discharged states.

these samples increase correspondingly, indicating a transition where Mn^{2+} coordination shifts from H_2O to acetamide as the acetamide content increases. This suggests competitive coordination, with Mn^{2+} showing a preference for acetamide molecules over H_2O. In Figure 2c, the coordination number between Mn^{2+} and ClO_4^- remains below 1 and is minimally affected by the acetamide content, indicating that ClO_4^- primarily resides in the second solvation shell. The molecular dynamics simulation snapshots of the Mn-ion eutectic electrolytes are illustrated in Figures 2d and S4−S7. The most probable solvation structure for Mn^{2+} in the MA-8 electrolyte is magnified in Figure 2e, illustrating that acetamide molecules play a central role in modifying the hydrogen-bonding network. As shown in Figure 2f, the binding energy of acetamide to Mn^{2+} is greater compared to those of acetamide-H_2O and H_2O−Mn^{2+} in the Mn-ion eutectic electrolyte system. Variations in the solvation structures of Mn-ion eutectic electrolytes are governed by the molar ratio of Mn^{2+} to acetamide and differences in binding energy. In Figure S8, statistical charts of the hydrogen bonding types and average numbers in the MA-4, MA-8, and MA-12 electrolytes demonstrate that the numbers of the hydrogen bonds related to H_2O−H_2O and ClO_4^-−H_2O significantly decreases with acetamide addition, indicating the reconstruction of the hydrogen bond network. As shown in Figure 2g, acetamide predominantly occupies the first solvation shell of Mn^{2+}, while ClO_4^- remains in the second shell due to weak interaction with Mn^{2+}. Increasing the content of acetamide in the electrolyte system induces a transition from a water-dominated to an acetamide-dominated solvation structure, significantly reducing the number of active H_2O molecules in the solvation shell. This transition is accompanied by a reduction in H_2O−H_2O hydrogen bonding, leading to a decrease in the number of active free water molecules and the reconstruction of the hydrogen bond network. These structural changes effectively contribute to expanding the ESW of the Mn-ion eutectic electrolyte.

Linear sweep voltammetry (LSV) measurements were conducted by using three-electrode setup to evaluate the ESW of the Mn-ion eutectic electrolytes (Figure 2h). As the molar ratio of Mn^{2+} to acetamide decreases from 1:4 to 1:12, the ESWs of the Mn-ion eutectic electrolytes expands from 2.43 to 3.24 V (versus Ag/AgCl), with a corresponding decrease in slope of the LSV curve. This broadening of the ESW is attributed to the effective inhibition of the hydrogen evolution reaction (HER) and oxygen evolution reaction (OER) at low and high potentials, respectively, due to the reduced free H_2O content. However, excessive acetamide does not significantly further expand the ESW and may negatively impact physical properties among the tested electrolytes, MA-8 demonstrates an optimal balance, with a wide ESW (2.91 V) and favorable properties, including high ionic conductivity (5.17 mS cm^{-1}), low viscosity (50.3 mPa s), low T_m (−78.9 °C), low water content (12.94 wt %, Figure S2). These characteristics suggest that the MA-8 electrolyte has the potential to improve electrochemical performance of Mn-ion batteries.

Electrochemical Properties of PTCDI Anodes in Mn-Ion Eutectic Electrolytes. PTCDI, a widely used organic material in pigments, dye-sensitized solar cells, and electro-

https://doi.org/10.1021/jacs.5c01639
J. Am. Chem. Soc. 2025, 147, 13721−13731

chemical energy storage devices,[40−44] shows great potential as an electrode for Mn^{2+} storage due to its abundant carbonyl groups and optimally sized aromatic rings. As illustrated in Figures S9−S11, the PTCDI powder exhibits a uniform structure with a nanorod morphology, confirmed by SEM and TEM images. The electrochemical properties of the PTCDI electrode were evaluated using a three-electrode setup with PTCDI electrode as the working electrode, Pt electrode as the counter electrode, Ag/AgCl electrode as the reference electrode and an MA-8 eutectic electrolyte. Cyclic voltammetry (CV) analysis, conducted at scan rates from 0.2 to 2.0 mV s^{-1}, reveals slight cathodic and anodic peak shifts (Figure 3a), indicating excellent reaction kinetics. Analysis of CV curves using the equation $i = av^b$ indicates a predominantly capacitive-controlled process with calculated b values nearing 1 at both redox potentials (Figure 3b). Moreover, separating capacitive and diffusion-limited contributions calculated using the equation $i(V) = k_1v + k_2v^{1/2}$ shows a capacitive contribution of up to 92.0%, which increases with scan rates (Figure 3c,d). The contribution ratios of capacitive process of the PTCDI electrode at scan rates of 0.2, 0.4, 0.6, 0.8, 1.0, 1.5, and 2.0 mV s^{-1} are calculated to be 74.3%, 78.7%, 86.3%, 88.6%, 90.8%, 91.4%, and 92.0%, respectively. This indicates that the PTCDI electrode provides sufficient diffusion channels for Mn^{2+} diffusion. The redox peak positions show minimal shift in the subsequent scans (Figure S12), suggesting that the redox processes of the PTCDI electrode in the MA-8 electrolyte are highly stable.

The PTCDI electrode demonstrates stable discharge capacities of 100.5 to 57.3 mAh g^{-1} across current densities of 0.2 to 5.0 A g^{-1}, with minimal degradation when returned to 0.2 A g^{-1} after high-rate cycling (Figure 3e). This capacity retention reflects a utilization of 73.6% to 41.9% relative to PTCDI's theoretical capacity (136.6 mAh g^{-1}) based on a two-electron carbonyl transfer. As shown in Figure 3f, the galvanostatic charge−discharge profiles of the PTCDI electrode at different current densities display two discharge plateaus at around −0.38 and −0.67 V (versus Ag/AgCl) and two charge plateaus at around −0.11 and −0.4 V (versus Ag/AgCl). At a current density of 0.5 A g^{-1}, the PTCDI electrode delivers an initial discharge capacity of 84.5 mAh g^{-1} and maintains 78.5 mAh g^{-1} after 300 cycles with a high-capacity retention of 93.5% (Figure 3g), corresponding to only 0.02% capacity fading per cycle. The charge−discharge profiles of first and 300th cycles illustrate that potential plateaus remain unchanged throughout the charge−discharge processes. In contrast, the PTCDI electrode demonstrates inferior cycling performance in saturated aqueous $Mn(ClO_4)_2$ electrolyte (without the addition of acetamide), exhibiting a low-capacity retention of 68.1% after 300 cycles at 0.5 A g^{-1} (Figure S13). This rapid capacity decay is primarily attributed to the dissolution of PTCDI electrode and the side reactions associated with abundant free water molecules in aqueous electrolyte. These results indicate that PTCDI electrodes exhibit excellent electrochemical reversibility in the Mn-ion eutectic electrolyte and a strong capability for Mn^{2+} storage.

Mn^{2+} Storage Mechanism Studies of PTCDI Anodes in Mn-Ion Eutectic Electrolytes. Density functional theory (DFT) calculations were performed to determine the energy levels of the highest occupied molecular orbital (HOMO) and the lowest unoccupied molecular orbital (LUMO) in PTCDI, providing insight into its active sites for Mn^{2+} storage. The calculated HOMO − LUMO gap of 2.535 eV (Figure 4a) suggests good electronic conductivity, advantageous for efficient Mn^{2+} storage kinetics. Simulated electrostatic potential mapping (Figure 4b) shows positive charges in the blue-shaded perylene core and negative charges concentrated around the carbonyl oxygen atoms, indicating carbonyl groups as active Mn^{2+} insertion sites during redox processes.

FTIR analysis (Figure 4c) reveals characteristic peaks: N−H vibrating at 3151 cm^{-1}, C═O stretching at 1670 cm^{-1}, C═C stretching from perylene units at 1572 cm^{-1}, and C−N bonds at 1360 and 1272 cm^{-1}. In the three-electrode cell, Mn^{2+} binds with PTCDI during the discharging steps and is released from PTCDI during the charging steps, within the potential range of 0.3 to −1.0 V versus the Ag/AgCl reference electrode. Ex situ FTIR spectra of PTCDI electrodes at different charge/discharge states (Figure 4d−f) illustrate structural evolution, where the peak intensity of the carbonyl group at 1670 cm^{-1} weakens during discharge, indicating conversion of C═O groups to $C-O^-$. A new absorption peak at 1643 cm^{-1} appears, attributed to the Mn^{2+} bonding with $C-O^-$. Upon recharging, the carbonyl peak gradually recovers, suggesting a reversible enolization reaction during the redox process.

To further examine structural changes due to enolization, in situ Raman spectra (Figure 4g) capture the PTCDI electrode's behavior at various charge/discharge states. The prominent Raman peaks observed at 1285, 1357, 1555, and 1570 cm^{-1} corresponding to C−C inter-ring, C−C single-bond, C═C symmetrical and C═C antisymmetrical stretching modes, shift to lower frequencies and weaken in intensity during discharge to −1 V. These peak positions and intensities fully recover upon recharging to 0.3 V versus Ag/AgCl. This is mainly owing to the reversible coordination and dissociation of Mn^{2+} with PTCDI molecule, leading to the formation and vanishment of free radical anions for PTCDI, and the carbon skeleton structure of PTCDI is also transformed accordingly. Additionally, the reversible loss and recovery of the C═O peak at 1595 cm^{-1} confirm the transformation of C═O to C−O−Mn and back, highlighting PTCDI's capability for Mn^{2+} storage via enolization.

The SEM image of the PTCDI electrode at the discharged state (Figure S14a) and the corresponding energy dispersive spectroscopy (EDS) mapping images confirm the presence of Mn in the PTCDI electrode at the discharged state (Figure S14b−d). Ex situ XPS analyses further demonstrate that Mn^{2+} binds with the carbonyl groups at the discharged state and is effectively released from PTCDI during the charging process. As depicted in Figure 4h, two intense peaks at 653.4 and 641.6 eV are attributed to Mn $2p_{1/2}$ and Mn $2p_{3/2}$ at the discharged state. These peaks nearly vanish at the charged state, indicating highly efficient binding and release of Mn^{2+} with PTCDI. Figure 4i illustrates O 1s XPS spectra across pristine, discharged, and charged states, with the O 1s peak shifting from 531.3 to 530.6 eV during discharge, corresponding to the C═O to $C-O^-$ conversion. This peak reverts upon charging, confirming the reversibility of the enolization reaction.

Electrochemical Performances of NiHCF||PTCDI Full Batteries Based on Mn-Ion Eutectic Electrolytes. For the construction of Mn-ion full batteries, a Prussian blue analogue NiHCF was synthesized and employed as cathode material to match with PTCDI anode material. The successful synthesis of NiHCF was confirmed by X-ray diffraction (XRD) analysis (Figure S15). SEM images reveal the morphology of the as-prepared NiHCF active material (Figure S16). The electrochemical properties of the NiHCF electrode in the MA-8

https://doi.org/10.1021/jacs.5c01639
J. Am. Chem. Soc. 2025, 147, 13721−13731

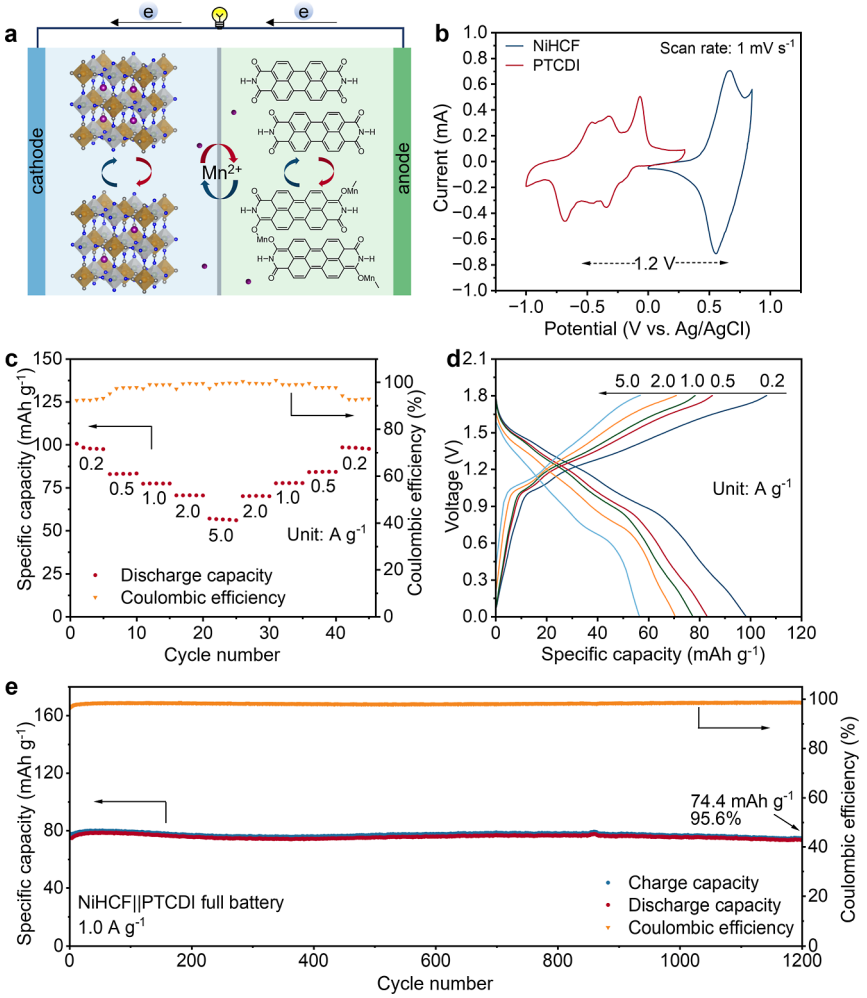

Figure 5. (a) Schematic illustration and working mechanism of the NiHCF||PTCDI full battery based on the MA-8 electrolyte. (b) CV curves of active materials and expected voltage plateau of the NiHCF||PTCDI full battery. (c) Rate performance of the NiHCF||PTCDI full battery at various current densities. (d) Galvanostatic charge−discharge profiles of the NiHCF||PTCDI full battery. (e) Cycling stability of the NiHCF||PTCDI full battery at a current density of 1.0 A g^{-1}.

electrolyte were evaluated in three-electrode cells, with the NiHCF electrode as the working electrode, a Pt electrode as the counter electrode, and an Ag/AgCl electrode as the reference electrode. When scanned at 1.0 mV s^{-1}, the NiHCF electrode exhibits an oxidation peak at 0.66 V (versus Ag/AgCl) and a reduction peak at 0.55 V (versus Ag/AgCl). The CV curves of the NiHCF electrode at different scan rates demonstrate excellent redox reversibility in the Mn-ion eutectic electrolyte (Figure S17a). The redox peak positions at the first cycle and the 10th cycle remain unchanged and overlapped (Figure S17b), indicating the excellent redox stability of NiHCF electrode in the MA-8 electrolyte. As shown in Figure S17c, the capacitive contribution ratios of NiHCF electrode at scan rates of 0.5, 1.0, 1.5, 2.0, and 5.0 mV s^{-1} are calculated to be 32.0%, 39.4%, 41.4%, 45.2%, and 59.6%, respectively. These results indicate that the Mn^{2+} storage in NiHCF electrode is primarily controlled by the diffusion effect, while the capacitive process also contributes to partial capacity. The galvanostatic charge−discharge profiles of the NiHCF electrode at different current densities display a discharge plateau at around 0.55 V (versus Ag/AgCl) and a charge plateau at around 0.65 V (versus Ag/AgCl) (Figure S17d). These results indicate that NiHCF is a promising active material for Mn^{2+} storage. The cycling performance of NiHCF electrode was evaluated in both MA-8 electrolyte and saturated aqueous $Mn(ClO_4)_2$ electrolyte (without acetamide) at a current density of 2.0 A g^{-1} (Figure S18). In MA-8 electrolyte, the NiHCF electrode maintains a discharge capacity of 35.9 mAh g^{-1} over 1000 cycles, demonstrating excellent compatibility and stability. In contrast, when tested in saturated aqueous $Mn(ClO_4)_2$ electrolyte, the initial discharge capacity of 35.1 mAh g^{-1} decreases significantly to 27.5 mAh g^{-1}, corresponding to a low-capacity retention of 78.3% after 1000 cycles. These results confirm the superior effectiveness of Mn-ion eutectic electrolyte in enhancing the cycling stability of NiHCF electrode compared to aqueous electrolyte.

The schematic illustration and working mechanism of Mn-ion full batteries, composed of the MA-8 electrolyte, PTCDI anodes, and NiHCF cathodes, are presented in Figure 5a. Based on the CV curves of PTCDI and NiHCF, the expected voltage plateau of the NiHCF||PTCDI full battery is approximately 1.2 V (Figure 5b). The rate performance of the NiHCF||PTCDI full battery was tested in the voltage range of 0−1.8 V (Figure 5c). The NiHCF||PTCDI full battery exhibits stable discharge capacities of 98.4, 83.1, 77.5, 70.6, and 56.7 mAh g^{-1} (calculated based on the weight of the PTCDI

https://doi.org/10.1021/jacs.5c01639
J. Am. Chem. Soc. 2025, 147, 13721−13731

active material) with high Coulombic efficiencies of 92.8%, 97.7%, 98.9%, 99.3% and 99.7% at various current densities of 0.2, 0.5, 1.0, 2.0, and 5.0 A g^{-1}, respectively. After the high-rate cycling process, the full battery shows negligible capacity degradation when the current density returns to 0.2 A g^{-1}, demonstrating excellent rate performance. The galvanostatic charge−discharge curves confirm that NiHCF||PTCDI full batteries maintain a stable voltage plateau of 1.2 V (Figure 5d). Long-term cycling at 1.0 A g^{-1} (Figure 5e) shows the discharge capacity of the full battery starting at 77.8 mAh g^{-1} and retaining 74.4 mAh g^{-1} after 1200 cycles, achieving a capacity retention of 95.6% and only 0.004% fading per cycle, indicating remarkable stability. The Coulombic efficiency of the full battery remains above 98% throughout, indicating effective inhibition of side reactions of the electrolyte and electrode materials. The charge−discharge profiles of NiHCF||PTCDI full battery during the 100th, 500th, 1000th, and 1200th cycles demonstrate minimal capacity degradation and only a tiny voltage shift during long-term cycling (Figure S19), confirming that the full battery can stably operate between 0 and 1.8 V. Background measurements on carbon paper and Ketjen Black indicated a discharge capacity of 8.7 mAh g^{-1} (Figure S20), indicating that very slight capacity of the full battery is attributed to current collector and conductive agent. The effects of different eutectic electrolytes on the electrochemical performance of full batteries were evaluated. The Nyquist plots show that the Ohmic impedance of NiHCF||PTCDI full batteries based on MA-4, MA-8, and MA-12 electrolytes are 5.7, 6.3, and 7.1 Ω cm^{-2}, respectively (Figure S21), indicating excellent electronic conductivity of the full battery. The above battery tests demonstrate that the excellent electrochemical performance of the Mn-ion full batteries based on hydrated eutectic electrolyte and conjugated organic anode has achieved a great breakthrough, which are very competitive among the existing aqueous Mn-ion battery systems (Table S2).

CONCLUSIONS

In conclusion, this work presents a sustainable, high-performance Mn-ion full battery system by successfully integrating a novel hydrated eutectic electrolyte and a PTCDI anode. The carefully designed electrolyte—composed of $Mn(ClO_4)_2 \cdot 6H_2O$ and acetamide—offers a wide electrochemical stability window (2.91 V), high ionic conductivity, cost-effectiveness (about 186 $/kg), and minimal toxicity, making it an environmentally friendly alternative. Spectroscopic characterizations and molecular dynamics simulations confirm the optimized solvation structure, which enhances Mn^{2+} transport while effectively reducing water reactivity. Additionally, the PTCDI anode demonstrates robust Mn^{2+} storage capacity through a reversible enolization redox process, providing exceptional cycling stability and rate performance. The resulting NiHCF||PTCDI full battery exhibits good rate capability (up to 5.0 A g^{-1}), a voltage plateau of 1.2 V, and excellent cycling stability over 1200 cycles at a current density of 1.0 A g^{-1} with a low capacity degradation rate of 0.004% per cycle. This study highlights the electrolyte's ability to address challenges associated with Mn-ion battery stability and establishes PTCDI as a viable anode material, advancing Mn-ion battery technology as a scalable, safe, and cost-effective energy storage solution.

ASSOCIATED CONTENT

Supporting Information

The Supporting Information is available free of charge at https://pubs.acs.org/doi/10.1021/jacs.5c01639.

Experimental section and additional figures and tables, including flammability test, molecular dynamics simulation snapshots, SEM images, TEM images, EDS mapping images, XRD test, CV curves, EIS curves, cycling preformance, battery performance comparisons, and stability tests (PDF)

AUTHOR INFORMATION

Corresponding Authors

Yichao Yan − *State Key Laboratory of Coordination Chemistry, MOE Key Laboratory of Mesoscopic Chemistry, MOE Key Laboratory of High Performance Polymer Materials and Technology, Jiangsu Key Laboratory of Advanced Organic Materials, Suzhou Key Laboratory of Green Intelligent Manufacturing of New Energy Materials and Devices, Tianchang New Materials and Energy Technology Research Center, Institute of Green Chemistry and Engineering, School of Sustainable Energy and Resources, School of Chemistry and Chemical Engineering, Nanjing University, Nanjing, Jiangsu 210023, P. R. China*; Email: ychyan@nju.edu.cn

Zhong Jin − *State Key Laboratory of Coordination Chemistry, MOE Key Laboratory of Mesoscopic Chemistry, MOE Key Laboratory of High Performance Polymer Materials and Technology, Jiangsu Key Laboratory of Advanced Organic Materials, Suzhou Key Laboratory of Green Intelligent Manufacturing of New Energy Materials and Devices, Tianchang New Materials and Energy Technology Research Center, Institute of Green Chemistry and Engineering, School of Sustainable Energy and Resources, School of Chemistry and Chemical Engineering, Nanjing University, Nanjing, Jiangsu 210023, P. R. China*; orcid.org/0000-0001-8860-8579; Email: zhongjin@nju.edu.cn

Authors

Tengfei Dai − *State Key Laboratory of Coordination Chemistry, MOE Key Laboratory of Mesoscopic Chemistry, MOE Key Laboratory of High Performance Polymer Materials and Technology, Jiangsu Key Laboratory of Advanced Organic Materials, Suzhou Key Laboratory of Green Intelligent Manufacturing of New Energy Materials and Devices, Tianchang New Materials and Energy Technology Research Center, Institute of Green Chemistry and Engineering, School of Sustainable Energy and Resources, School of Chemistry and Chemical Engineering, Nanjing University, Nanjing, Jiangsu 210023, P. R. China*

Binze Yang − *State Key Laboratory of Coordination Chemistry, MOE Key Laboratory of Mesoscopic Chemistry, MOE Key Laboratory of High Performance Polymer Materials and Technology, Jiangsu Key Laboratory of Advanced Organic Materials, Suzhou Key Laboratory of Green Intelligent Manufacturing of New Energy Materials and Devices, Tianchang New Materials and Energy Technology Research Center, Institute of Green Chemistry and Engineering, School of Sustainable Energy and Resources, School of Chemistry and Chemical Engineering, Nanjing University, Nanjing, Jiangsu 210023, P. R. China*

https://doi.org/10.1021/jacs.5c01639
J. Am. Chem. Soc. 2025, 147, 13721−13731

Jie Wei − *State Key Laboratory of Coordination Chemistry, MOE Key Laboratory of Mesoscopic Chemistry, MOE Key Laboratory of High Performance Polymer Materials and Technology, Jiangsu Key Laboratory of Advanced Organic Materials, Suzhou Key Laboratory of Green Intelligent Manufacturing of New Energy Materials and Devices, Tianchang New Materials and Energy Technology Research Center, Institute of Green Chemistry and Engineering, School of Sustainable Energy and Resources, School of Chemistry and Chemical Engineering, Nanjing University, Nanjing, Jiangsu 210023, P. R. China*

Xinmei Song − *State Key Laboratory of Coordination Chemistry, MOE Key Laboratory of Mesoscopic Chemistry, MOE Key Laboratory of High Performance Polymer Materials and Technology, Jiangsu Key Laboratory of Advanced Organic Materials, Suzhou Key Laboratory of Green Intelligent Manufacturing of New Energy Materials and Devices, Tianchang New Materials and Energy Technology Research Center, Institute of Green Chemistry and Engineering, School of Sustainable Energy and Resources, School of Chemistry and Chemical Engineering, Nanjing University, Nanjing, Jiangsu 210023, P. R. China*

Pengbo Zhang − *State Key Laboratory of Coordination Chemistry, MOE Key Laboratory of Mesoscopic Chemistry, MOE Key Laboratory of High Performance Polymer Materials and Technology, Jiangsu Key Laboratory of Advanced Organic Materials, Suzhou Key Laboratory of Green Intelligent Manufacturing of New Energy Materials and Devices, Tianchang New Materials and Energy Technology Research Center, Institute of Green Chemistry and Engineering, School of Sustainable Energy and Resources, School of Chemistry and Chemical Engineering, Nanjing University, Nanjing, Jiangsu 210023, P. R. China*

Yuzhu Liu − *State Key Laboratory of Coordination Chemistry, MOE Key Laboratory of Mesoscopic Chemistry, MOE Key Laboratory of High Performance Polymer Materials and Technology, Jiangsu Key Laboratory of Advanced Organic Materials, Suzhou Key Laboratory of Green Intelligent Manufacturing of New Energy Materials and Devices, Tianchang New Materials and Energy Technology Research Center, Institute of Green Chemistry and Engineering, School of Sustainable Energy and Resources, School of Chemistry and Chemical Engineering, Nanjing University, Nanjing, Jiangsu 210023, P. R. China*

Sheng Wen − *State Key Laboratory of Coordination Chemistry, MOE Key Laboratory of Mesoscopic Chemistry, MOE Key Laboratory of High Performance Polymer Materials and Technology, Jiangsu Key Laboratory of Advanced Organic Materials, Suzhou Key Laboratory of Green Intelligent Manufacturing of New Energy Materials and Devices, Tianchang New Materials and Energy Technology Research Center, Institute of Green Chemistry and Engineering, School of Sustainable Energy and Resources, School of Chemistry and Chemical Engineering, Nanjing University, Nanjing, Jiangsu 210023, P. R. China*

Huan Li − *State Key Laboratory of Coordination Chemistry, MOE Key Laboratory of Mesoscopic Chemistry, MOE Key Laboratory of High Performance Polymer Materials and Technology, Jiangsu Key Laboratory of Advanced Organic Materials, Suzhou Key Laboratory of Green Intelligent Manufacturing of New Energy Materials and Devices, Tianchang New Materials and Energy Technology Research Center, Institute of Green Chemistry and Engineering, School of Sustainable Energy and Resources, School of Chemistry and Chemical Engineering, Nanjing University, Nanjing, Jiangsu 210023, P. R. China*

Tianchen Yu − *State Key Laboratory of Coordination Chemistry, MOE Key Laboratory of Mesoscopic Chemistry, MOE Key Laboratory of High Performance Polymer Materials and Technology, Jiangsu Key Laboratory of Advanced Organic Materials, Suzhou Key Laboratory of Green Intelligent Manufacturing of New Energy Materials and Devices, Tianchang New Materials and Energy Technology Research Center, Institute of Green Chemistry and Engineering, School of Sustainable Energy and Resources, School of Chemistry and Chemical Engineering, Nanjing University, Nanjing, Jiangsu 210023, P. R. China*

Zuoxiu Tie − *State Key Laboratory of Coordination Chemistry, MOE Key Laboratory of Mesoscopic Chemistry, MOE Key Laboratory of High Performance Polymer Materials and Technology, Jiangsu Key Laboratory of Advanced Organic Materials, Suzhou Key Laboratory of Green Intelligent Manufacturing of New Energy Materials and Devices, Tianchang New Materials and Energy Technology Research Center, Institute of Green Chemistry and Engineering, School of Sustainable Energy and Resources, School of Chemistry and Chemical Engineering, Nanjing University, Nanjing, Jiangsu 210023, P. R. China*

Huapeng Sun − *School of New Energy, Chenjiang Laboratory, Chenzhou Vocational Technical College, Chenzhou, Hunan 423000, China*

Complete contact information is available at: https://pubs.acs.org/10.1021/jacs.5c01639

Notes

The authors declare no competing financial interest.

■ ACKNOWLEDGMENTS

The authors appreciate the financial support from the National Natural Science Foundation of China (22479074 and 22475096), the General Project of the Joint Fund of Equipment Preresearch and the Ministry of Education (8091B02052407), the Natural Science Foundation of Jiangsu Province (BK20240400 and BK20241236), the Science and Technology Major Project of Jiangsu Province (BG2024013), the Scientific and Technological Achievements Transformation Special Fund of Jiangsu Province (BA2023037), the Academic Degree and Postgraduate Education Reform Project of Jiangsu Province (JGKT24_C001), the Key Core Technology Open Competition Project of Suzhou City (SYG2024122), the open research fund of Suzhou Laboratory (SZLAB-1308-2024-TS005), the Gusu Leading Talent Program of Scientific and Technological Innovation and Entrepreneurship of Wujiang District in Suzhou City (ZXL2021273), and the Chenzhou National Sustainable Development Agenda Innovation Demonstration Zone Provincial Special Project (2023sfq11).

■ REFERENCES

(1) Zhang, J.; Zhang, H.; Weng, S.; Li, R.; Lu, D.; Deng, T.; Zhang, S.; Lv, L.; Qi, J.; Xiao, X.; Fan, L.; Geng, S.; Wang, F.; Chen, L.; Noked, M.; Wang, X.; Fan, X. Multifunctional Solvent Molecule Design Enables High-Voltage Li-Ion Batteries. *Nat. Commun.* **2023**, *14* (1), 2211.

(2) Zheng, S.; Shi, D.; Sun, T.; Zhang, L.; Zhang, W.; Li, Y.; Guo, Z.; Tao, Z.; Chen, J. Hydrogen Bond Networks Stabilized High-Capacity

Organic Cathode for Lithium-Ion Batteries. *Angew. Chem., Int. Ed.* **2023**, *62* (9), No. e202217710.
(3) Liu, F.; Gao, L.; Zhang, Z.; Zhang, L.; Deng, N.; Zhao, Y.; Kang, W. Interfacial Challenges, Processing Strategies, and Composite Applications for High Voltage All-Solid-State Lithium Batteries Based on Halide and Sulfide Solid-State Electrolytes. *Energy Storage Mater.* **2024**, *64*, 103072.
(4) Zhang, S.; Zhao, F.; Chen, J.; Fu, J.; Luo, J.; Alahakoon, S. H.; Chang, L.; Feng, R.; Shakouri, M.; Liang, J.; Zhao, Y.; Li, X.; He, L.; Huang, Y.; Sham, T.; Sun, X. A Family of Oxychloride Amorphous Solid Electrolytes for Long-Cycling All-Solid-State Lithium Batteries. *Nat. Commun.* **2023**, *14* (1), 3780.
(5) Dong, S.; Sheng, L.; Wang, L.; Liang, J.; Zhang, H.; Chen, Z.; Xu, H.; He, X. Challenges and Prospects of All-Solid-State Electrodes for Solid-State Lithium Batteries. *Adv. Funct. Mater.* **2023**, *33* (49), 2304371.
(6) Men, L.; Feng, S.; Zhang, J.; Luo, X.; Zhou, Y. A Systematic Review of Efficient Recycling for the Cathode Materials of Spent Lithium-Ion Batteries: Process Intensification Technologies beyond Traditional Methods. *Green Chem.* **2024**, *26* (3), 1170−1193.
(7) Xu, X.; Han, X.; Lu, L.; Wang, F.; Yang, M.; Liu, X.; Wu, Y.; Tang, S.; Hou, Y.; Hou, J.; Yu, C.; Ouyang, M. Challenges and Opportunities toward Long-Life Lithium-Ion Batteries. *J. Power Sources* **2024**, *603*, 234445.
(8) Jiang, L.; Han, S.; Hu, Y.; Yang, Y.; Lu, Y.; Lu, Y.; Zhao, J.; Chen, L.; Hu, Y. Rational Design of Anti-Freezing Electrolytes for Extremely Low-Temperature Aqueous Batteries. *Nat. Energy* **2024**, *9* (7), 839−848.
(9) Wang, Y.; Ou, T.; Dong, Y.; Chen, L.; Huang, Y.; Sun, D.; Qiang, W.; Pei, X.; Li, Y.; Tan, Y. A Green Asymmetric Bicyclic Co-Solvent Molecule for High-Voltage Aqueous Lithium-Ion Batteries. *Adv. Mater.* **2024**, *36* (15), 2311009.
(10) Liang, Y.; Dong, H.; Aurbach, D.; Yao, Y. Current Status and Future Directions of Multivalent Metal-Ion Batteries. *Nat. Energy* **2020**, *5* (9), 646−656.
(11) Wei, C.; Song, J.; Wang, Y.; Tang, X.; Liu, X. Recent Development of Aqueous Multivalent-Ion Batteries Based on Conversion Chemistry. *Adv. Funct. Mater.* **2023**, *33* (45), 2304223.
(12) Liu, Y.; He, G.; Jiang, H.; Parkin, I.; Shearing, P.; Brett, D. Cathode Design for Aqueous Rechargeable Multivalent Ion Batteries: Challenges and Opportunities. *Adv. Funct. Mater.* **2021**, *31* (13), 2010445.
(13) Jiao, Z.; Cai, X.; Wang, X.; Li, Y.; Bie, Z.; Song, W. Trace Amount of Nitrilotriacetate Induced Electrolyte Evolution and Textured Surface for Stable Zn Anode. *Adv. Energy Mater.* **2023**, *13* (48), 2302676.
(14) Sun, C.; Huang, G.; Xu, C.; Li, L.; Tang, A.; Zhou, X.; Wang, J.; Pan, F. Improved Compatibility of Aqueous Electrolyte with TiO_2(B) toward High-Voltage Aqueous Rechargeable Mg-Ion Batteries. *Energy Storage Mater.* **2024**, *66*, 103197.
(15) Zhang, S.; Zhu, Y.; Ren, S.; Li, C.; Chen, X.; Li, Z.; Han, Y.; Shi, Z.; Feng, S. Covalent Organic Framework with Multiple Redox Active Sites for High-Performance Aqueous Calcium Ion Batteries. *J. Am. Chem. Soc.* **2023**, *145* (31), 17309−17320.
(16) Zhang, X.; Wei, H.; Li, S.; Ren, B.; Jiang, J.; Qu, G.; Lv, H.; Liang, G.; Chen, G.; Zhi, C.; Li, H.; Liu, Z. Manipulating Coordination Environment for a High-Voltage Aqueous Copper-Chlorine Battery. *Nat. Commun.* **2023**, *14* (1), 6738.
(17) Hu, E.; Jia, B.; Zhu, Q.; Xu, J.; Loh, X.; Chen, J.; Pan, H.; Yan, Q. Engineering High Voltage Aqueous Aluminum-Ion Batteries. *Small* **2024**, 2309252.
(18) Shen, D.; Zheng, X.; Luo, R.; Jiang, T.; Wang, M.; Zhang, M.; Peng, Q.; Song, L.; Zhou, S.; Hou, Z.; Qian, Y.; Chen, W. A Rechargeable, Non-Aqueous Manganese Metal Battery Enabled by Electrolyte Regulation. *Joule* **2024**, *8* (3), 780−798.
(19) Lei, J.; Yao, Y.; Wang, Z.; Lu, Y. Towards High-Areal-Capacity Aqueous Zinc−Manganese Batteries: Promoting MnO_2 Dissolution by Redox Mediators. *Energy Environ. Sci.* **2021**, *14* (8), 4418−4426.
(20) Lei, J.; Jiang, L.; Lu, Y. Emerging Aqueous Manganese-Based Batteries: Fundamental Understanding, Challenges, and Opportunities. *Chem. Phys. Rev.* **2023**, *4* (2), 021307.
(21) Wang, M.; Meng, Y.; Xu, Y.; Shen, D.; Tong, P.; Chen, W. An Energetic Aqueous Mn Metal Anode. *ACS Energy Lett.* **2024**, *9* (4), 1381−1388.
(22) Bi, S.; Wang, S.; Yue, F.; Tie, Z.; Niu, Z. A Rechargeable Aqueous Manganese-Ion Battery Based on Intercalation Chemistry. *Nat. Commun.* **2021**, *12* (1), 6991.
(23) Bi, S.; Zhang, Y.; Deng, S.; Tie, Z.; Niu, Z. Proton-Assisted Aqueous Manganese-Ion Battery Chemistry. *Angew. Chem., Int. Ed.* **2022**, *61* (17), No. e202200809.
(24) Nimkar, A.; Chae, M.; Wee, S.; Bergman, G.; Gavriel, B.; Turgeman, M.; Malchik, F.; Levi, M.; Sharon, D.; Lukatskaya, M.; Shpigel, N.; Mandler, D. What About Manganese? Toward Rocking Chair Aqueous Mn-Ion Batteries. *ACS Energy Lett.* **2022**, *7* (12), 4161−4167.
(25) Cai, L.; Lu, L.; Lan, Y.; Zhang, Y.; Wang, J.; Lin, Z.; Li, R.; Zhang, F.; Yu, J.; Lu, W.; Bai, X.; Wang, W. Multidentate Chelation Enables High-Efficiency Mn^{2+} Storage in Polyimide Covalent Organic Framework for Aqueous All Mn-Ion Battery. *Adv. Energy Mater.* **2023**, *13* (37), 2301631.
(26) Yang, Q.; Qu, X.; Cui, H.; He, X.; Shao, Y.; Zhang, Y.; Guo, X.; Chen, A.; Chen, Z.; Zhang, R.; Kong, D.; Shi, Z.; Liu, J.; Qiu, J.; Zhi, C. Rechargeable Aqueous Mn-Metal Battery Enabled by Inorganic-Organic Interfaces. *Angew. Chem., Int. Ed.* **2022**, *61* (35), No. e202206471.
(27) Wang, M.; Meng, Y.; Xu, Y.; Chen, N.; Chuai, M.; Yuan, Y.; Sun, J.; Liu, Z.; Zheng, X.; Zhang, Z.; Li, D.; Chen, W. Aqueous All-Manganese Batteries. *Energy Environ. Sci.* **2023**, *16* (11), 5284−5293.
(28) Liu, F.; Zhang, Y.; Li, G.; Jiang, J.; Chen, L.; Song, T.; Pei, Y.; Wang, X.; Wu, X.; Long, B. Hydrated Eutectic Electrolyte Promotes the Preferential Growth of Zn (0 0 2) Plane and Suppresses Side Reaction for High-Stability Zinc Anodes. *Chem. Eng. J.* **2024**, *493*, 152526.
(29) Wang, G.; Fu, H.; Lu, J.; Huang, S.; Pei, C.; Min, D.; Zhang, Q.; Park, H. Gradient-Structured and Robust Solid Electrolyte Interphase In Situ Formed by Hydrated Eutectic Electrolytes for High-Performance Zinc Metal Batteries. *Adv. Energy Mater.* **2024**, *14* (8), 2303549.
(30) Luo, X.; Wang, R.; Zhang, L.; Liu, Z.; Li, H.; Mao, J.; Zhang, S.; Hao, J.; Zhou, T.; Zhang, C. Air-Stable and Low-Cost High-Voltage Hydrated Eutectic Electrolyte for High-Performance Aqueous Aluminum-Ion Rechargeable Battery with Wide-Temperature Range. *ACS Nano* **2024**, *18* (20), 12981−12993.
(31) Zhang, X.; Wang, R.; Liu, Z.; Ma, Q.; Li, H.; Liu, Y.; Hao, J.; Zhang, S.; Mao, J.; Zhang, C. Regulated Hydrated Eutectic Electrolyte Enhancing Interfacial Chemical Stability for Highly Reversible Aqueous Aluminum-Ion Battery with a Wide Temperature Range of − 20 to 60 °C. *Adv. Energy Mater.* **2024**, *14* (22), 2400314.
(32) Hao, J.; Yuan, L.; Zhu, Y.; Bai, X.; Ye, C.; Jiao, Y.; Qiao, S. Low-cost and Non-flammable Eutectic Electrolytes for Advanced Zn-I_2 Batteries. *Angew. Chem., Int. Ed.* **2023**, *62* (39), No. e202310284.
(33) Zhu, Y.; Guo, X.; Lei, Y.; Wang, W.; Emwas, A. H.; Yuan, Y.; He, Y.; Alshareef, H. Hydrated Eutectic Electrolytes for High-Performance Mg-Ion Batteries. *Energy Environ. Sci.* **2022**, *15* (3), 1282−1292.
(34) Lu, C.; Wang, Z.; Zhang, Y.; Tang, G.; Wang, Y.; Guo, X.; Li, J.; Wei, L. Aqueous Aluminum-Zinc Hybrid Ion Batteries with Urea-Based Hydrated Eutectic Electrolytes. *Nano Energy* **2024**, *120*, 109158.
(35) Qu, K.; Lu, X.; Jiang, N.; Wang, J.; Tao, Z.; He, G.; Yang, Q.; Qiu, J. Eutectic Electrolytes Convoying Low-Temperature Metal-Ion Batteries. *ACS Energy Lett.* **2024**, *9* (3), 1192−1209.
(36) Geng, L.; Wang, X.; Han, K.; Hu, P.; Zhou, L.; Zhao, Y.; Luo, W.; Mai, L. Eutectic Electrolytes in Advanced Metal-Ion Batteries. *ACS Energy Lett.* **2022**, *7* (1), 247−260.
(37) Li, J.; Lou, Y.; Zhou, S.; Chen, Y.; Zhao, X.; Azizi, A.; Lin, S.; Fu, L.; Han, C.; Su, Z.; Pan, A. Intrinsically Decoupled Coordination

https://doi.org/10.1021/jacs.5c01639
J. Am. Chem. Soc. 2025, 147, 13721−13731

Chemistries Enable Quasi-Eutectic Electrolytes with Fast Kinetics toward Enhanced Zinc-Ion Capacitors. *Angew. Chem., Int. Ed.* **2024**, *63*, No. e202406906.
(38) Wang, S.; Chen, S.; Ying, Y.; Li, G.; Wang, H.; Cheung, K.; Meng, Q.; Huang, H.; Ma, L.; Zapien, J. Fast Reaction Kinetics and Commendable Low-Temperature Adaptability of Zinc Batteries Enabled by Aprotic Water-Acetamide Symbiotic Solvation Sheath. *Angew. Chem., Int. Ed.* **2024**, *63* (8), No. e202316841.
(39) Qiu, K.; Ma, G.; Wang, Y.; Liu, M.; Zhang, M.; Li, X.; Qu, X.; Yuan, W.; Nie, X.; Zhang, N. Highly Compact Zinc Metal Anode and Wide-Temperature Aqueous Electrolyte Enabled by Acetamide Additives for Deep Cycling Zn Batteries. *Adv. Funct. Mater.* **2024**, *34* (18), 2313358.
(40) Rostami-Tapeh-Esmail, E.; Golshan, M.; Salami-Kalajahi, M.; Roghani-Mamaqani, H. Perylene-3,4,9,10-Tetracarboxylic Diimide and Its Derivatives: Synthesis, Properties and Bioapplications. *Dyes Pigm.* **2020**, *180*, 108488.
(41) Shen, Z.; Eickemeyer, F.; Gao, J.; Pfeifer, L.; Bradford, D.; Freitag, M.; Zakeeruddin, S.; Grätzel, M. Molecular Engineering of Low-Cost, Efficient, and Stable Photosensitizers for Dye-Sensitized Solar Cells. *Chem* **2023**, *9* (12), 3637−3647.
(42) Jiang, L.; Lu, Y.; Zhao, C.; Liu, L.; Zhang, J.; Zhang, Q.; Shen, X.; Zhao, J.; Yu, X.; Li, H.; Huang, X.; Chen, L.; Hu, Y. Building Aqueous K-Ion Batteries for Energy Storage. *Nat. Energy* **2019**, *4* (6), 495−503.
(43) Jiang, L.; Lu, Y. Building a Long-Lifespan Aqueous K-Ion Battery Operating at − 35 °C. *ACS Energy Lett.* **2024**, *9* (3), 985−991.
(44) Brown, J.; Karlsmo, M.; Bendadesse, E.; Johansson, P.; Grimaud, A. Exploring the Electrochemistry of PTCDI for Aqueous Lithium-Ion Batteries. *Energy Storage Mater.* **2024**, *66*, 103218.

https://doi.org/10.1021/jacs.5c01639
J. Am. Chem. Soc. 2025, 147, 13721−13731